Frequency-domain analysis of photoacoustic imaging data from prostate adenocarcinoma tumors in a murine model

Ronald E. Kumon[*], Cheri X. Deng[*], Xueding Wang[†]

[*]Department of Biomedical Engineering, University of Michigan, Ann Arbor, Michigan 48109, USA; [†]Department of Radiology, University of Michigan, Ann Arbor, MI 48109, USA

Address all correspondence to: cxdeng@umich.edu and xdwang@umich.edu

Abstract

Photoacoustic imaging is an emerging technique for anatomical and functional sub-surface imaging, but previous studies have predominantly focused on time-domain analysis. In this study, frequency-domain analysis of the radio-frequency signals from photoacoustic imaging was performed to generate quantitative parameters for tissue characterization. To account for the response of the imaging system, the photoacoustic spectra were calibrated by dividing the photoacoustic spectra (radio-frequency ultrasound spectra resulting from laser excitation) from tissue by the photoacoustic spectrum of a point absorber excited under the same conditions. The resulting quasi-linear photoacoustic spectra were fit by linear regression, and midband fit, slope, and intercept were computed from the best-fit line. These photoacoustic spectral parameters were compared between the region-of-interests (ROIs) representing prostate adenocarcinoma tumors and adjacent normal flank tissue in a murine model. The mean midband fit and intercept in the ROIs showed significant differences between cancerous and non-cancerous regions. These initial results suggest that such frequency-domain analysis can provide a quantitative method for tumor tissue characterization using photoacoustic imaging in vivo.

INTRODUCTION

Photoacoustic (PA) imaging is a nonionizing and noninvasive optical imaging modality that provides good soft tissue contrast, excellent spatial resolution, and deep penetration depth (Wang 2009). In their simplest form, PA images can be constructed by displaying only the amplitude of the envelope of the underlying radio-frequency (RF) photoacoustic signals received by a broad bandwidth ultrasound transducer as image brightness, similar to conventional B-mode ultrasound imaging. However, images generated this way or using other general PA imaging methods are subjected to the effects of a variety of factors including the optical excitation, US transducer response, and image post-processing, rendering the results operator- and system-dependent. Hence in order to generate images that represent only tissue properties and permit easy comparison of images obtained with different settings or systems methods need to be developed to remove or minimize these factors.

Similar problems exist in traditional pulse-echo ultrasound (US) imaging with both acoustical excitation and detection (Shung and Thieme 1993). Frequency-domain analysis of backscattered RF signals in pulse-echo US imaging (Lizzi et al. 1983; Feleppa et al. 1986; Lizzi et al. 1987; Insana and Brown 1993; Insana et al. 1994; Lizzi et al. 2003) has been exploited for objective, quantitative tissue characterization. In this approach, the power spectra of the RF signals from a region of interest are computed and calibrated to remove the system input and output effects. Because the resulting US spectra are often quasilinear over the bandwidth used in typical US imaging, a linear regression is performed to obtain a relatively small set of parameters from the calibrated US spectra (e.g., slope and intercept of regression line and the midband fit, which is the linear function evaluated at the midpoint of the usable bandwidth). It has been shown theoretically that these parameters are related to tissue microstructural properties (e.g.,

effective acoustic scatterer size and concentration) (Lizzi 1997). This quantitative US approach has proven to be effective for identifying changes in tissue state for prostate, breast, and other cancer tissue (Golub et al. 1993; Feleppa et al. 2001; Silverman et al. 2003; Oelze et al. 2004; Feleppa 2008) as well as intravascular plaque (Nasu et al. 2006) and has even been implemented to perform real-time tissue-typing (Lizzi et al. 2003). We hypothesize that PA spectral parameters may have similar interpretation and utility. For example, the amplitude of PA pressure pulse from a uniformly-illuminated spherical object is proportional to the optical absorption coefficient and size of the object, while the signal duration is proportional to its radius (Diebold 2009) and frequency-domain analysis of PA RF data from blood vessel phantoms (ink-filled cylindrical tubes in gelatin) has shown a relationship between spectrum characteristics and cylinder diameter (Gertsch et al. 2010). Frequency-domain analysis of high-frequency photoacoustic imaging of ex vivo ocular tissue with visible light excitation has shown changes in midband fit and slope around pigmented iris (Silverman et al. 2010). Thus it is reasonable to expect that the size, concentration, distribution, and efficiency of optical absorbers will be expressed in the PA spectral properties from tissue in vivo, particularly given the prevalence of endogenous optical absorbers like hemoglobin. The goal of this pilot study is to determine whether frequency-domain analysis of RF data from PA imaging could be used to obtain numerical parameters for tissue characterization in the context of prostate-cancer tumors in a murine model.

MATERIALS AND METHODS

Experiment

A schematic diagram of the imaging system is shown in Fig. 1A. Laser illumination (752 nm) from a neodymium-doped yttrium aluminium garnet (Nd:YAG) pumped optical

parametric oscillator (OPO) laser (Vibrant B, Opotek) with a pulse duration of 5.5 ns and an incident energy density of 13 mJ/cm^2 was incident from the top (along the Z-axis) while the US signal was acquired from the side. A commercial US unit (z.one, Zonare) with a 128-element L10-5 linear-array transducer (5 MHz receiving –40 dB bandwidth centered at 6.25 MHz) synchronized with the laser was used to detect the PA signal. The ultrasound probe was coupled to the exfoliated rat flank using ultrasonic coupling gel. With the US probe placed in the X-Y plane, the imaging plane was orthogonal to the direction of light illumination. With similar depth beneath the skin surface, each point in the imaging plane had similar light fluence. When growing tumors develop inefficient neovasculature and/or necrotic core, they may exhibit an increase in deoxygenated hemoglobin. Excitation at 752 nm was thus chosen to take advantage of the peak of the ratio of the molar optical absorption coefficient of deoxygenated hemoglobin over oxygenated hemoglobin around this optical wavelength. To generate PA images, 257 RF lines sampled at 40 Msamples/s were formed from the 128-channel IQ data, where the interval between two adjacent lines was 0.15 mm (i.e. half pitch). Conventional B-mode US images were separately acquired using the same probe.

The calibration measurement used for PA spectral analysis was performed by imaging a hair fiber with a diameter of 30 μm, as shown in Fig. 1B. The photoacoustic signal from the hair fiber was generated using the same light illumination geometry with the same incident energy density as those in the animal experiment. The hair fiber was 25 mm from the US probe and absorption of the PA signal in the phantom is negligible. With a small diameter much less than the wavelength at the center frequency of the probe (0.24 mm), the hair fiber illuminated with the laser beam formed a point PA source with a broadband PA signal.

In vivo imaging experiment was performed on 7 rats (Dunning R-3327, 200–250 g, Charles River Laboratory) under an animal protocol approved by our University Committee on Use and Care of Animals. This rat model is the most widely used animal prostate cancer model, and the Metastatic Anaplastic Tumor able to disseminate to Lymph nodes and Lung (MatLyLu) subline is commonly used in assessing the therapeutic effect of cancer therapies. This Dunning tumor line has been reported to possess morphology and physiology that are similar to human prostate cancer (Isaacs et al. 1981; Lucia et al. 1998). The subcutaneous MatLyLu tumors were induced by injecting 1×10^5 MatLyLu cells (ATCC) suspended in 0.05 mL PBS into the shaved rat flank. Imaging was conducted 9–12 days after inoculation when tumors with a surface diameter of 5–10 mm and a thickness of 2–4 mm had been generated and enhanced angiogenesis had also started (Kragh et al. 2001).

Data analysis

The beamformed RF data from PA imaging was imported into MATLAB-based (v. 2009a, Mathworks) software developed in our lab for US spectral analysis that had been modified for PA image reconstruction and data analysis (Kumon et al. 2007; Kumon et al. 2010). For the tumor, rectangular regions of interest (ROIs) were selected based on the apparent location of the tumor in the corresponding co-registered US image. Registration of the US and PA images of the same tissue region was performed by (1) finding the transformation to align the fiber location in the US and PA images of the phantom-embedded hair and (2) applying the same transformation to the tissue images. For comparison, rectangular ROIs for normal (non-prostate) tissue were chosen 2 mm lateral to the tumor ROI with the same general area and as close as possible to the same depth as the original tumor ROI (while maintaining the ROI under the curved skin surface) to minimize any differences in ultrasonic attenuation of the PA signal

between ROIs. The mean area of all ROIs was 0.56 ± 0.12 cm^2. The range to all ROIs was 20 to 30 mm from the probe and beyond its minimal recommended imaging distance. Within the ROI, the signals of each RF data line were gated by a series of sliding Hamming windows (to minimize effects of spectral leakage) of 1.5 µs (~2.3 mm), each offset by 0.1 µs (~0.15 mm). The PA power spectra were calculated using fast Fourier transform (FFT) within each gated segment and converted to a dB scale.

To remove system artifacts, the PA power spectrum from a hair fiber was subtracted from each PA power spectrum to obtain the calibrated PA spectrum. Linear regression of the calibrated PA power spectra was performed over the usable bandwidth for the system, defined as the range of frequencies within −15 dB of the peak of the PA power spectrum of the hair fiber, to generate the slope, intercept, and midband fit. The mean of each PA spectral parameter was computed from all the windowed segments in the ROI. The mean ROI values from all animals were then analyzed using Student's T-test to determine if there were significant differences ($p < 0.05$) between the tumor and normal ROIs. If Levene's test for equality of variances indicated $p < 0.05$, then the T-test was performed with unequal variances assumed. The Shapiro-Wilk statistic was used to test the assumption of normality made by the T-test. Statistical calculations were performed using SPSS (v. 16, SPSS).

RESULTS

Figures 2A and 2B shows typical results of the tumor area in PA images (red) and co-registered US images (grayscale) for two different animals. For orientation, the US probe is located above the top of the image, while the laser illumination is mostly normal to the plane of the figure slightly angled toward the top. In both cases the PA images, which are sensitive to

hemoglobin content, highlight the vasculature surrounding the tumor core, which is indicated by the central hypoechoic region on US image.

Figure 3 shows the PA spectral analysis procedure. A segment of the time-domain PA signal from the hair fiber, before (black) and after (red) windowing with the Hamming window (Fig. 3A), centered at the hair fiber (inset of Fig. 3A) (the transducer was at the left of the fiber) was used to compute its PA power spectrum (Fig. 3B). The −15 dB bandwidth was from 2.5 to 6.8 MHz. Figure 3C shows a segment of the time-domain signal for the PA data acquired in the tumor in Fig. 2A, before (black) and after (red) windowing. The inset indicates the location of the RF line using the same orientation as in Fig. 3A. Figure 3D shows the corresponding PA power spectrum for the windowed data in Fig. 3C. The inset shows the calibrated PA power spectrum with the best-fit line (dashed red) from a linear regression over the usable bandwidth to yield slope, intercept, and midband fit of the PA spectrum (indicated by the dashed horizontal line at the midband). This procedure was repeated for each segment of RF data in each ROI.

To graphically display the PA spectral information, parametric image maps were constructed, as shown in the example of Fig. 4. For reference, Fig. 4A shows the US image of the same tumor as in Fig. 2B with the ROIs for the tumor and normal tissue superimposed. Figures 4B, 4C, and 4D show the image maps for the midband fit, slope, and intercept, respectively, of the calibrated PA power spectra. In these images, the pixel corresponding to the center of each signal window is assigned a color based on the PA spectral value in that window, and the result is superimposed on the co-registered US grayscale image. For this particular case, Figs. 4B and 4D show that the mean midband fit and mean intercept increase in the tumor ROI as compared to the normal ROIs (−28.5 dB vs. −42.6 dB [left] and −38.1 dB [right] for midband

fit, −47.8 dB vs. −58.5 dB [left] and −50.0 dB [right] for intercept), while the mean slope decreases (4.2 dB/MHz vs. 3.4 dB/MHz [left] and 2.6 dB/MHz [right]).

Table 1 shows the statistical results of the PA spectral data analysis and PA images for all animals ($n = 7$) in the study. The data is reported as the mean ± standard deviation of the mean values over each ROI. Both the normal and tumor groups satisfied the Shapiro-Wilk test for normality. The mean values of midband fit and intercept were significantly different between the normal and tumor ROIs. The mean slope was lower for the normal tissue but the difference was not statistically significant. No significant differences were observed between the left and right normal ROIs for any of the PA spectral parameters.

DISCUSSION

PA imaging has been demonstrated to be a useful tool for identifying blood flow *in vivo*, and may be valuable for better detecting the presence of the angiogenesis typically associated with tumor formation. As seen in Fig. 2, the tumor is largely identified in the US images by the presence of a hypoechoic (probably necrotic) core. However, tumor cells likely extend beyond this core to regions which are not readily apparent in the US image. The current results suggest that the primary difference between the cancerous tumor and surrounding normal tissue is an enhanced PA signal, as quantified by the ~9 dB increase in the mean PA midband fit. The enhanced PA signal is most likely due to the increased optical absorption resulting from the increase in the hemoglobin concentration associated with angiogenesis near the tumor. When combined with the morphological information from the US image and/or US spectral parameters, it may be possible to achieve improved diagnosis with the additional, complementary information about the extent of the tumor or possibly even to distinguish between different tumor types based on differences in frequency-domain PA parameters. The use of exogenous contrast

agents targeted to tumor cells may be able to further enhance this capability (Rajian et al. 2009; Yao et al. 2009; Zhang et al. 2009; Lu et al. 2010).

The typical qualitative presentation of PA images uses only the amplitude of the envelope of the RF-data to produce grayscale images, where frequency and phase information of the signals that may include potentially useful information about tissue properties were not used. The grayscale values are subjected to the settings of a variety of system- and user-dependent factors (e.g. brightness/contrast, thresholding, time-gain compensation adjustments, etc.) that make it difficult to compare between studies under different experimental conditions. The frequency-domain method described herein utilizes the unaltered RF data and yields parameters that compensate for system response and can be applied to PA data from any US imaging system.

This study has several limitations. First, while the spectral parameters of pulse-echo US signals are related to tissue properties such as the spatial variation in acoustic impedance, the corresponding correlation between PA spectral and optical microstructural parameters has yet to be determined. A detailed theoretical investigation combined with a PA study of phantoms with scatterers of known acoustic and optical parameters will help to elucidate this relationship. Second, the performance of PA spectral analysis may be improved by using a US system that is specifically designed to capture the signals of broad bandwidth expected in PA imaging. Finally, the spatial averaging inherent in an ROI method limits the spatial resolution over which the PA spectral parameters can be computed.

REFERENCES

Diebold GJ. Photoacoustic monopole radiation: Waves from objects with symmetry in one, two, and three dimensions. In: Wang LV, ed. Photoacoustic imaging and spectroscopy. New York: CRC Press, 2009. pp 3-17.

Feleppa EJ. Ultrasonic tissue-type imaging of the prostate: Implications for biopsy and treatment guidance. Cancer Biomark 2008;4:201-212.

Feleppa EJ, Ennis RD, Schiff PB, Wuu CS, Kalisz A, Ketterling J, Urban S, Liu T, Fair WR, Porter CR and others. Spectrum-analysis and neural networks for imaging to detect and treat prostate cancer. Ultrason Imaging 2001;23:135-146.

Feleppa EJ, Lizzi FL, Coleman DJ, Yaremko MM. Diagnostic spectrum analysis in ophthalmology: A physical perspective. Ultrasound Med Biol 1986;12:623-631.

Gertsch AG, Bush NL, Birtill DCC, Bamber JC. Towards characterising the size of microscopic optical absorbers using optoacoustic emission spectroscopy. In: Oraevsky AA, Wang LV, eds. Photons plus ultrasound: Imaging and sensing 2010, Proc SPIE, Vol 7564. Bellingham, WA: SPIE, 2010.

Golub RM, Parsons RE, Sigel B, Feleppa EJ, Justin J, Zaren HA, Rorke M, Sokil-Melgar J, Kimitsuki H. Differentiation of breast tumors by ultrasonic tissue characterization. J Ultrasound Med 1993;12:601-608.

Insana MF, Brown DG. Acoustic scattering theory applied to soft biological tissues. In: Shung KK, ed. Ultrasonic scattering in biological tissues. Boca Raton, FL: CRC Press, 1993. pp 75-124.

Insana MF, Hall TJ, Cook LT. Backscatter coefficient estimation using array transducers. IEEE Trans Ultrason Ferroelectr Freq Control 1994;41:714-723.

Isaacs JT, Yu GW, Coffey DS. The characterization of a newly identified, highly metastatic variety of Dunning R 3327 rat prostatic adenocarcinoma system: the MAT LyLu tumor. Invest Urol 1981;19:20-23.

Kragh M, Quistorff B, Lund EL, Kristjansen PE. Quantitative estimates of vascularity in solid tumors by non-invasive near-infrared spectroscopy. Neoplasia 2001;3:324-330.

Kumon RE, Olowe K, Faulx AL, Farooq FT, Chen VK, Zhou Y, Wong RC, Isenberg GA, Sivak MV, Chak A and others. EUS spectrum analysis for in vivo characterization of pancreatic and lymph node tissue: A pilot study. Gastrointest Endosc 2007;66:1096-1106.

Kumon RE, Pollack MJ, Faulx AL, Olowe K, Farooq FT, Chen VK, Zhou Y, Wong RC, Isenberg GA, Sivak MV and others. In vivo characterization of pancreatic and lymph node tissue by using EUS spectrum analysis: A validation study. Gastrointest Endosc 2010;71:53-63.

Lizzi FL. Ultrasonic scatterer-property images of the eye and prostate. In: Schneider SC, Levy M, McAvoy BR, eds. Proc 1997 IEEE Ultrasonics Symp. Piscataway, NJ: IEEE, 1997. pp 1109-1116.

Lizzi FL, Feleppa EJ, Alam SK, Deng CX. Ultrasonic spectrum analysis for tissue evaluation. Pattern Recog Lett 2003;24:637-658.

Lizzi FL, Greenebaum M, Feleppa EJ, Elbaum M, Coleman DJ. Theoretical framework for spectrum analysis in ultrasonic tissue characterization. J Acoust Soc Am 1983;73:1366-1373.

Lizzi FL, Ostromogilsky M, Feleppa EJ, Rorke MC, Yaremko MM. Relationship of ultrasonic spectral parameters to features of tissue microstructure. IEEE Trans Ultrason Ferroelectr Freq Control 1987;34:319-329.

Lu W, Huang Q, Geng KB, Wen XX, Zhou M, Guzatov D, Brecht P, Su R, Oraevsky A, Wang LV and others. Photoacoustic imaging of living mouse brain vasculature using hollow gold nanospheres. Biomaterials 2010;31:2617-2626.

Lucia MS, Bostwick DG, Bosland M, Cockett AT, Knapp DW, Leav I, Pollard M, Rinker-Schaeffer C, Shirai T, Watkins BA. Workgroup I: Rodent models of prostate cancer. Prostate 1998;36:49-55.

Nasu K, Tsuchikane E, Katoh O, Vince DG, Virmani R, Surmely JF, Murata A, Takeda Y, Ito T, Ehara M and others. Accuracy of in vivo coronary plaque morphology assessment: a validation study of in vivo virtual histology compared with in vitro histopathology. J Am Coll Cardiol 2006;47:2405-2412.

Oelze ML, O'Brien WD, Jr., Blue JP, Zachary JF. Differentiation and characterization of rat mammary fibroadenomas and 4T1 mouse carcinomas using quantitative ultrasound imaging. IEEE Trans Med Imaging 2004;23:764-771.

Rajian JR, Carson PL, Wang X. Quantitative photoacoustic measurement of tissue optical absorption spectrum aided by an optical contrast agent. Opt Express 2009;17:4879-4889.

Shung KK, Thieme GA, eds. Ultrasonic scattering in biological tissues. Boca Raton, Florida: CRC Press, 1993.

Silverman RH, Folberg R, Rondeau MJ, Boldt HC, Lloyd HO, Chen X, Lizzi FL, Weingeist TA, Coleman DJ. Spectral parameter imaging for detection of prognostically significant histologic features in uveal melanoma. Ultrasound Med Biol 2003;29:951-959.

Silverman RH, Kong F, Lloyd HO, Chen VC. Fine-resolution photoacoustic imaging of the eye. In: Oraevsky AA, Wang LV, eds. Photons plus ultrasound: Imaging and sensing 2010, Proc SPIE, Vol 7564. Bellingham, WA: SPIE, 2010.

Wang LV, ed. Photoacoustic Imaging and Spectroscopy. New York: CRC Press, 2009.

Yao JJ, Maslov K, Hu S, Wang LHV. Evans blue dye-enhanced capillary-resolution photoacoustic microscopy in vivo. Journal of Biomedical Optics 2009;14:054049.

Zhang Q, Iwakuma N, Sharma P, Moudgil BM, Wu C, McNeill J, Jiang H, Grobmyer SR. Gold nanoparticles as a contrast agent for in vivo tumor imaging with photoacoustic tomography. Nanotechnology 2009;20:395102.

FIGURE CAPTIONS

Fig. 1. Schematic diagram of experimental apparatus. (US: Ultrasound, PC: Personal computer, Nd:YAG: Neodymium-doped Yttrium Aluminium Garnet, OPO: Optical Parametric Oscillator)

Fig. 2. Example images showing PA images (red) and the co-registered US images (grayscale) for tumors in two different animals. The PA images highlight the tumor vasculature. Scale bars indicate 5 mm.

Fig. 3. Procedure for spectral analysis of PA data. (A) Signal from hair fiber without (black) and with (red) a 1.5-μs Hamming window applied. The inset shows the PA image where the horizontal line indicates the data segment in the plot. Scale bar indicates 1 mm. (B) Power spectrum of the windowed data in Fig. 3A. (C) Signal from the tumor region with same graph parameters as in Fig. 3A. (D) Power spectrum of the windowed data in Fig. 3C. The inset shows the calibrated power spectrum, the corresponding best-fit line from the linear regression (dashed red), and the midband fit (horizontal dashed black).

Fig. 4. Spectral parametric image maps from the PA data in Fig. 2B. (A) US image shows the ROIs selected for the tumor and normal tissue. The PA image maps are superimposed on the US image for (B) midband fit [dB], (C) slope [dB/MHz], and (D) intercept [dB]. The color bar below each image map shows the range of the parameter for the ROIs. The dynamic range for the PA and US signals is 16 bits.

TABLE CAPTION

Table 1. Descriptive statistics and hypothesis testing for comparison of tumor and normal ROIs.

Table 1

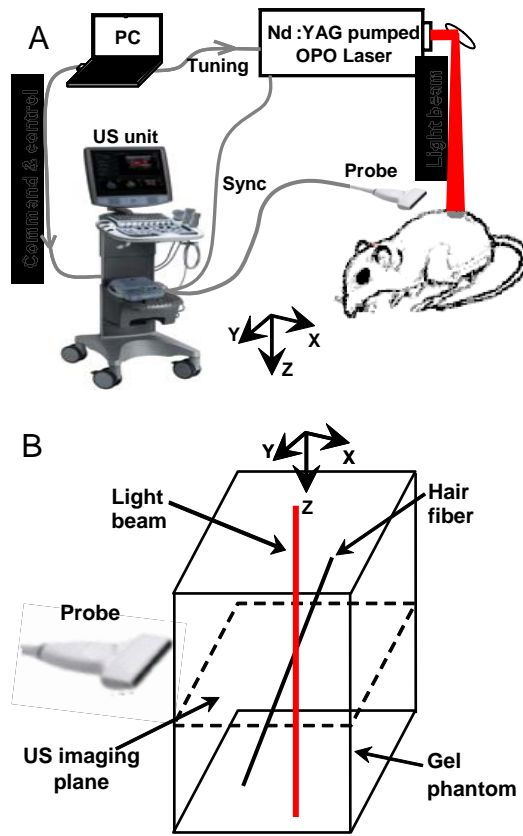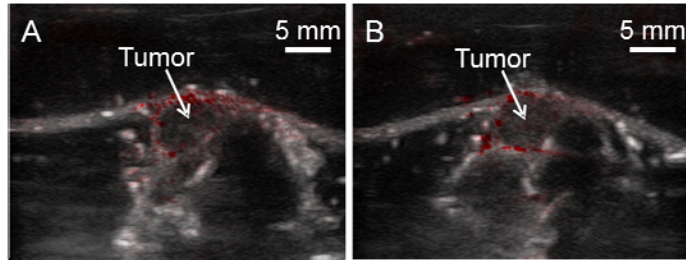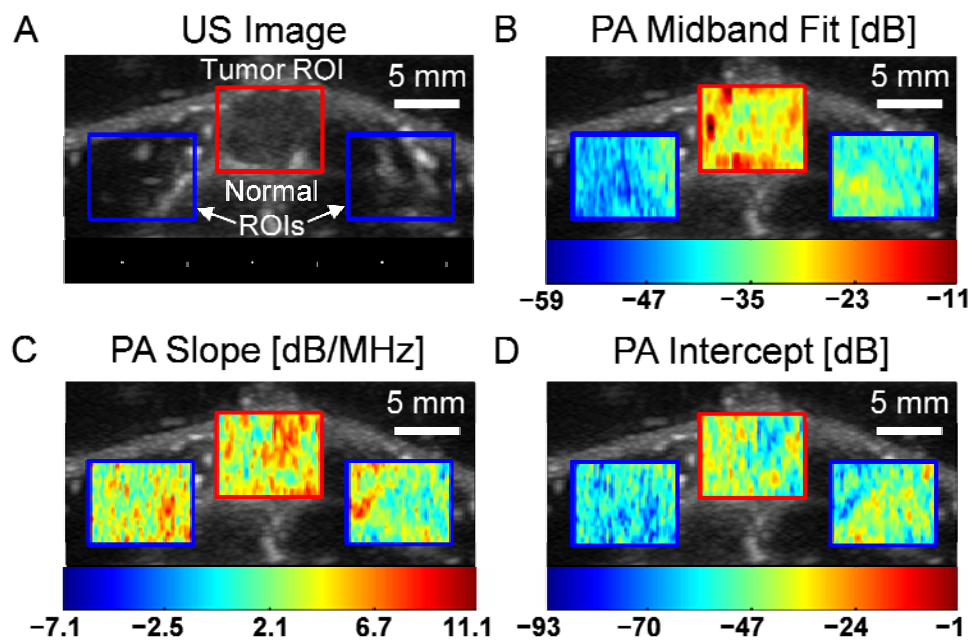| Spectral Parameter	Normal (*n* = 14)	Tumor (*n* = 7)	*T*-test (*p*-value)
PA Midband Fit [dB]	−34.8±5.4	−26.0±2.6	< 0.001
PA Slope [dB/MHz]	3.8±1.6	4.3±0.3	0.312
PA Intercept [dB]	−52.6±9.2	−45.9±2.2	0.022

Figure 1

Figure 2

Figure 3

Figure 4